Original Paper

3D reverse-time migration for pure P-wave in orthorhombic media

Ying-Hui Liu [a], Jian-Ping Huang [a, *], Liang Chen [a], Qiang Mao [a], Kun Tian [b]

[a] *School of Geoscience, China University of Petroleum (East China), Qingdao, 266580, Shandong, China*
[b] *Geophysical Research Institute, Shengli Oilfield Company, SINOPEC, Dongying, 257022, Shandong, China*

ARTICLE INFO

ABSTRACT

Compared with the transverse isotropic (TI) medium, the orthorhombic anisotropic medium has both horizontal and vertical symmetry axes and it can be approximated as a set of vertical fissures developed in a group of horizontal strata. Although the full-elastic orthorhombic anisotropic wave equation can accurately simulate seismic wave propagation in the underground media, a huge computational cost is required in seismic modeling, migration, and inversion. The conventional coupled pseudo-acoustic wave equations based on acoustic approximation can be used to significantly reduce the cost of calculation. However, these equations usually suffer from unwanted shear wave artifacts during wave propagation, and the presence of these artifacts can significantly degrade the imaging quality. To solve these problems, we derived a new pure P-wave equation for orthorhombic media that eliminates shear wave artifacts while compromising computational efficiency and accuracy. In addition, the derived equation involves pseudo-differential operators and it must be solved by 3D FFT algorithms. In order to reduce the number of 3D FFT, we utilized the finite difference and pseudo-spectral methods to conduct 3D forward modeling. Furthermore, we simplified the equation by using elliptic approximation and implemented 3D reverse-time migration (RTM). Forward modeling tests on several homogeneous and heterogeneous models confirm that the accuracy of the new equation is better than that of conventional methods. 3D RTM imaging tests on three-layer and SEG/EAGE 3D salt models confirm that the ORT media have better imaging quality.

1. Introduction

Anisotropy is an important factor to be considered for accurate seismic imaging. Ignoring anisotropy can lead to significant distortions such as the blurring of migrated events, misaligned reflectors, and abnormal reflection coefficients. Many efforts have been made to study the anisotropic effects on seismic data and to include anisotropy in seismic forward modeling and migration (Wang et al., 2022a,b). Crampin and Evans (1984) summarized a unified theory for extensive dilatancy anisotropy (EDA), which analyzes and explains the causes of azimuthal anisotropy and predicts its universality. Although azimuthal anisotropy is more complex than polar anisotropy, introducing it into seismic inversion provides more effective information about fractured reservoirs. Postma (1955) introduced the periodic thin layer anisotropy (PTL) media, where each layer in an interlayer sequence is very thin with its thickness comparable to the main wavelength of the seismic wave. These multiple thin layers introduce anisotropic effects for seismic propagation. HTI (transversely isotropy with a horizontal symmetry axis, HTI) and VTI (transversely isotropy with a vertical symmetry axis, VTI) can approximate the fracture-induced EDA and PTL respectively. Combining EDA media and PTL media generates orthorhombic anisotropic (ORT) media in arbitrary directions (Bush and Crampin, 1991). VTI and HTI media are special cases of ORT media. In cases where vertically oriented fractures are developed on thin interbeds, or two sets of vertically oriented fracture systems are formed in the same stratum under different in-situ stress, EDA or PTL alone cannot describe their properties well. The ORT media is the most appropriate model to match such properties.

Compared to the elastic wave equation, the acoustic wave equation is commonly used for seismic forward modeling, imaging and inversion due to its lower computational cost. However, using the acoustic wave equation is inaccurate to describe the propagation of seismic waves because the actual seismic subsurface is anisotropic. To improve the accuracy of the acoustic equation,

Alkhalifah, 1998, 2000, 2003 proposed an acoustic approximation that sets the S-wave velocity along the symmetry axis to zero based on the weak dependence of P-wave propagation on S-wave velocity. This method utilized the fourth-order quasi-acoustic wave equations for VTI media and ORT media in the time-space domain. Following Alkhalifah's works, efforts have been made to further develop the formulation and optimize the algorithm for modeling and RTM. Zhou et al. (2006a, 2006b) decomposed the fourth-order equation of TI media into two coupled second-order equations under acoustic approximation, and extended the coupled equations to TTI (tilted transverse isotropic) media. Du et al. (2008), Fowler et al. (2010), Duveneck et al. (2008, 2011) derived different forms of coupled pseudo-acoustic wave equations in TI and ORT media (Du, 2004; Fowler and King, 2011; Cheng and Kang, 2014; Zhang and Zhang, 2011; and others), and implemented the RTM.

Unfortunately, these equations suffer from an inherent problem that the S-wave energy cannot be eliminated cleanly, resulting in the presence of S-wave artifacts in the wavefield. This leads to numerical dispersion and instability in areas with rapid variations of anisotropy parameters. Fletcher et al. (2009) suggested retaining a finite S-wave velocity in the coupling equations as a partial solution to the instability problem. However, this approach can increase the intensity of shear wave noise, and worsen the numerical dispersion with increasing recurrence time. Yoon et al. (2010) proposed to reduce the instability by setting $\varepsilon = \delta$ where the dip angle varies sharply, but this approach changes the kinematic characteristics of the wavefield and the local characteristics of the model. Other scholars have proposed various methods to solve this problem, such as putting sources into the isotropic or elliptic anisotropic layers (Alkhalifah, 2000), smoothing the anisotropy parameters model before seismic forward modeling or RTM (Zhang and Zhang, 2008), and applying noise suppressing filters (Zhang et al., 2009; Guan et al., 2011), and more. Unfortunately, none of these methods can fully eliminate shear wave artifacts and instability issues well.

The pure P-wave equations have been derived by removing the coupling relationship between the P- and S-wave, resulting in a pure P-wave wavefield that eliminates shear wave artifacts in modeling or RTM results. Liu et al. (2009) further simplified the P-wave dispersion relation in acoustic VTI media by using the optimal decomposition approximation method to derive the decoupled acoustic wave equation. Zhan et al. (2012) obtained the pure P-wave equation in the wavenumber domain using the square root approximation, and implemented the TTI RTM using the pseudo-spectral method (PSM) in space and rapid expansion method (REM) in time, yielding high-quality imaging results. Xu and Zhou (2014) decomposed the pseudo-differential operator into a differ-

et al. (2017) implemented an indirect pure P-wave wavefield extrapolation using low-rank decomposition. Mu et al. (2019, 2020a, 2020b) proposed a least-squares reverse-time migration method (LSRTM) based on the pure P-wave equation in TTI media that can correct the waveform distortion. Xu et al. (2020) proposed a new acoustic symmetry (AS) approximation for VTI media that aims to eliminate the coupled shear wave artifacts. Subsequently, Abedi and Stovas (2020) analyzed the rationality of the AS approximation method in detail and extended it to ORT media. In addition, Stovas et al. (2016, 2020, 2021a, 2021b, 2021c) have also done a lot of research in TI and ORT media.

In this paper, we derive a new pure P-wave equation that avoids shear wave artifacts for simulation and reverse-time migration in orthorhombic media. First, we derive a dispersion relation for P-wave in orthorhombic media by following the elastic Christoffel equation and introducing an acoustic approximation. Then, a series of mathematical transformations are performed on the dispersion relation to obtain the pure P-wave equation. Finally, we use a hybrid scheme (Du et al., 2015; Wang et al., 2020) that combines the finite difference method for solving a partial derivative in time and three partial derivatives in space, with the pseudo-spectral method for computing three mixed wave-number terms to obtain a pure P-wave wavefield. Moreover, we simplify the equation based on elliptic approximation and implement the 3D RTM with graphic processing unit (GPU) acceleration in order to reduce the large computational costs.

2. Theory

In constitutive coordinates, the stiffness tensor c_{ijkl} that is represented nine independent elastic parameters for orthorhombic media (The orthorhombic media model can be seen in Fig. 1) can be written as

$$C_{ORT} = \begin{pmatrix} c_{11} & c_{12} & c_{13} & & & \\ c_{12} & c_{22} & c_{23} & & & \\ c_{13} & c_{23} & c_{33} & & & \\ & & & c_{44} & & \\ & & & & c_{55} & \\ & & & & & c_{66} \end{pmatrix} \quad (1)$$

If the properties of the orthorhombic are identical in all vertical or horizontal planes, the orthorhombic media is reduced to TI media and the nine parameters are reduced to five.

Under generalized Hooke's law and Newton's second law, the 3D elastic second-order wave equation without the source term for orthorhombic media in the time-space domain is given by

$$\rho \frac{\partial^2 u}{\partial t^2} = c_{11} \frac{\partial^2 u}{\partial x^2} + c_{66} \frac{\partial^2 u}{\partial y^2} + c_{55} \frac{\partial^2 u}{\partial z^2} + (c_{12} + c_{66}) \frac{\partial^2 v}{\partial x \partial y} + (c_{13} + c_{55}) \frac{\partial^2 w}{\partial x \partial z}$$

$$\rho \frac{\partial^2 v}{\partial t^2} = c_{66} \frac{\partial^2 v}{\partial x^2} + c_{22} \frac{\partial^2 v}{\partial y^2} + c_{44} \frac{\partial^2 v}{\partial z^2} + (c_{12} + c_{66}) \frac{\partial^2 u}{\partial x \partial y} + (c_{23} + c_{44}) \frac{\partial^2 w}{\partial y \partial z} \quad (2)$$

$$\rho \frac{\partial^2 w}{\partial t^2} = c_{55} \frac{\partial^2 w}{\partial x^2} + c_{44} \frac{\partial^2 w}{\partial y^2} + c_{33} \frac{\partial^2 w}{\partial z^2} + (c_{13} + c_{55}) \frac{\partial^2 u}{\partial x \partial z} + (c_{23} + c_{44}) \frac{\partial^2 v}{\partial y \partial z}$$

ential operator and a scalar operator and implemented the forward simulation of TTI media in the time-space domain using the finite difference method (FDM), thereby improving the computational efficiency. This equation was further extended to ORT media. Huang

where u, v, and w are the wavefield of the three components; x, y, and z are three directions in Cartesian coordinates. Therefore, after the Fourier transform, Eq. (2) in the frequency-wavenumber domain can be shown as follows:

$$\rho\omega^2 \begin{bmatrix} \widehat{u} \\ \widehat{v} \\ \widehat{w} \end{bmatrix} = \begin{bmatrix} c_{11}k_x^2 + c_{66}k_y^2 + c_{55}k_z^2 & (c_{12} + c_{66})k_x k_y & (c_{13} + c_{55})k_x k_z \\ (c_{12} + c_{66})k_x k_y & c_{66}k_x^2 + c_{22}k_y^2 + c_{44}k_z^2 & (c_{23} + c_{44})k_y k_z \\ (c_{13} + c_{55})k_x k_z & (c_{23} + c_{44})k_y k_z & c_{55}k_x^2 + c_{44}k_y^2 + c_{33}k_z^2 \end{bmatrix} \begin{bmatrix} \widehat{u} \\ \widehat{v} \\ \widehat{w} \end{bmatrix} \tag{3}$$

where $\widehat{u}$, $\widehat{v}$, and $\widehat{w}$ are the wavefield in Fourier domain; k_x, k_y, and k_z are the wavenumber in the x, y, and z directions, respectively; ω is the angular frequency, and ρ is the density. Assuming that the solution of the plane wave for the elastic wave equation is

$$\boldsymbol{U} = \boldsymbol{P}\exp\left[i(xk_x + yk_y + zk_z - \omega t)\right] \tag{4}$$

where $\boldsymbol{U} = (u, v, w)^{\mathrm{T}}$, $\boldsymbol{P} = (p_x, p_y, p_z)^{\mathrm{T}}$ is the polarization vector of the plane wave. We can obtain the elastic Christoffel equation in orthorhombic media by plugging it into Eq. (3), namely

$$\boldsymbol{CP} = 0 \tag{5}$$

where

directions of particle polarization). By solving this equation, the phase velocities and corresponding mass polarization vectors can be obtained. However, solving the analytical expression for the phase velocity in any direction of propagation in three dimensions is complex, especially in low-symmetric media where the phase velocity varies along different directions of propagation. Typically, the analytical expression for phase velocity can only be given for a specific plane (symmetry plane) or a specific direction of propagation (axis of symmetry). For Eq. (5) to have a non-zero solution, the Christoffel matrix determinant must be zero, which can be expressed as

$$det\,[\boldsymbol{C}] = 0 \tag{6}$$

which results in a cubic dispersion equation of the form in orthorhombic media, and a representation of phase velocity is obtained

$$\boldsymbol{C} =$$
$$\begin{bmatrix} \left(c_{11}k_x^2 + c_{66}k_y^2 + c_{55}k_z^2\right) - \rho\omega^2 & (c_{12} + c_{66})k_x k_y & (c_{13} + c_{55})k_x k_z \\ (c_{12} + c_{66})k_x k_y & \left(c_{66}k_x^2 + c_{22}k_y^2 + c_{44}k_z^2\right) - \rho\omega^2 & (c_{23} + c_{44})k_y k_z \\ (c_{13} + c_{55})k_x k_z & (c_{23} + c_{44})k_y k_z & \left(c_{55}k_x^2 + c_{44}k_y^2 + c_{33}k_z^2\right) - \rho\omega^2 \end{bmatrix}$$

.

The Christoffel equation is used to determine the eigenvalues (the phase velocity of P-, SV-, and SH-wave) and eigenvectors (the

after solving (The relevant solution process can be referred to in Appendix A).
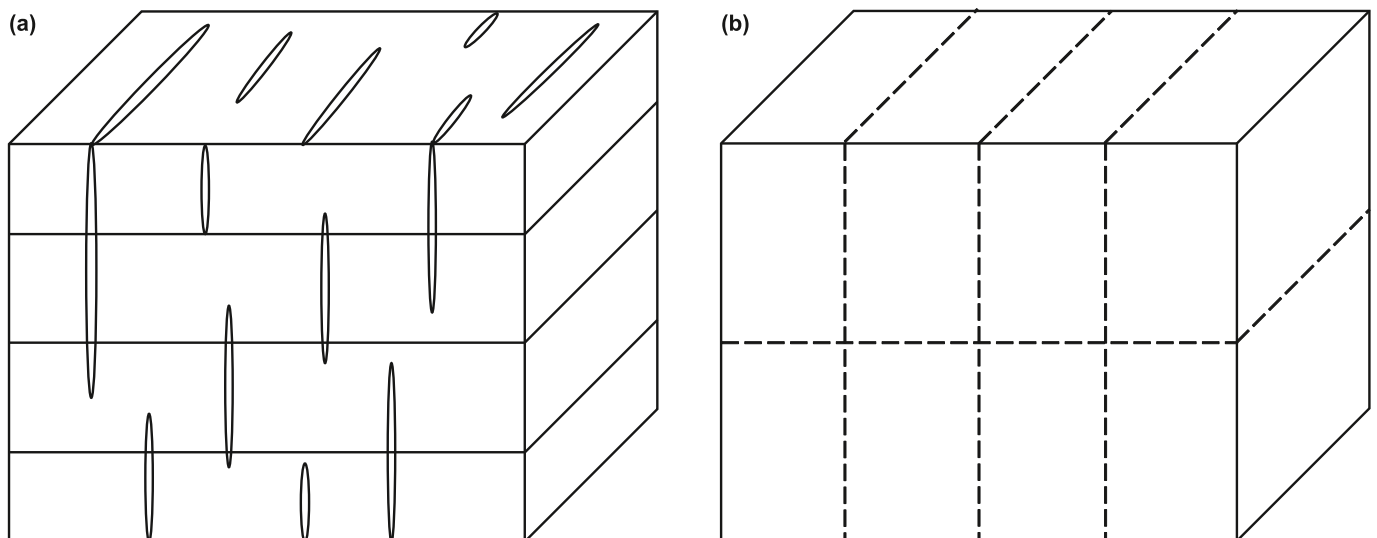
Fig. 1. Model of ORT anisotropic media: **(a)** fissure; **(b)** axis of symmetry.

$$\omega^2 = \frac{1}{\rho}\left[2\sqrt{\frac{-D}{3}}\cos\left(\frac{\beta}{3}+k\frac{2\pi}{3}\right) - A \Big/ 3\right], \qquad k = 0, 1, 2 \qquad (7)$$

The equation has a maximum root when $k = 0$, which corresponds to the phase velocity of the P-wave. Additionally, with $k = 1$ or 2, the two roots of the equation correspond to the phase velocity of the split shear waves. In isotropic media, the eigenvalues corresponding to the two S-wave components are identical, meaning the two S-wave components propagate with the same phase velocity and polarization direction. However, in anisotropic media, Eq. (5) does not have identical roots in the usual cases, which means that the two S-waves propagate with different phase velocities and polarization directions, resulting in a splitting phenomenon of the shear wave. In particular directions, the split S-wave propagates with the same phase velocity and polarization direction, leading to shear-wave singularities.

By applying the weak-anisotropic approximation to Eq. (7) (setting $\cos(\beta) = 1$ when $k = 0$), we can obtain the weak-anisotropic approximation expression for the phase velocity of the P-wave (Further details of the derivation can be found in Appendix B).

$$
\begin{aligned}
V^2 = V_{P0}^2[&1 + 2\varepsilon_2 \sin^4\theta\cos^4\phi + 2\varepsilon_1\sin^4\theta\sin^4\phi + 2\delta_2\sin^2\theta\cos^2\phi\cos^2\theta \\
&+ 2\delta_1\sin^2\theta\sin^2\phi\cos^2\theta + 2(2\varepsilon_2+\delta_3)\sin^4\theta\cos^2\phi\sin^2\phi]
\end{aligned}
\qquad (8)
$$

where θ is angle between the propagation direction and the vertical axis, and ϕ is angle between the propagation direction and the horizontal axis.

Describing the physical significance of the phase velocity of wave propagation in terms of the elastic stiffness tensor can be unintuitive. To address this issue, Thomsen has proposed a set of anisotropic parameters (Thomsen parameters) to characterize VTI media (Thomsen, 1986). These parameters provide a visual representation of some of the anisotropic characteristics of the media. Tsvankin extended this approach to orthorhombic media, introducing two vertical velocities and seven dimensionless parameters to characterize the elastic properties of orthorhombic media (Tsvankin, 1997),

$$
\begin{cases}
V_{P0} = \sqrt{\dfrac{c_{33}}{\rho}} & V_{S0} = \sqrt{\dfrac{c_{55}}{\rho}} & \gamma_1 = \dfrac{c_{66}-c_{55}}{2c_{55}} & \gamma_2 = \dfrac{c_{66}-c_{44}}{2c_{44}} \\[3mm]
\varepsilon_1 = \dfrac{c_{22}-c_{33}}{2c_{33}} & \varepsilon_2 = \dfrac{c_{11}-c_{33}}{2c_{33}} & \delta_1 = \dfrac{(c_{23}+c_{44})^2-(c_{33}-c_{44})^2}{2c_{33}(c_{33}-c_{44})} \\[3mm]
\delta_2 = \dfrac{(c_{13}+c_{55})^2-(c_{33}-c_{55})^2}{2c_{33}(c_{33}-c_{55})} & \delta_3 = \dfrac{(c_{12}+c_{66})^2-(c_{11}-c_{66})^2}{2c_{11}(c_{11}-c_{66})}
\end{cases}
$$

where V_{P0} is the velocity of the vertical P-wave; V_{S0} is the velocity

of the vertical S-wave; ε are parameters that determine the strength of the P-wave anisotropy, which indicate the difference between the horizontal and vertical phase velocities of the P-wave; γ are parameters that determine the strength of the S-wave anisotropy, which indicate the difference between the horizontal and vertical phase velocities of the S-wave; δ are transitional parameters linking the vertical and horizontal phase velocities of the P-wave, which indicate the magnitude of the anisotropy of the phase velocity near the vertical direction of the P-wave.

Eq. (7) is considered to be complicated for forward simulation and RTM, therefore, setting $V_{S0} = 0$ for the purpose of saving calculation costs, and the stiffness tensors are then reduced to

$$
\begin{cases}
c_{11} = \rho(1+2\varepsilon_2)V_{P0}^2 & c_{22} = \rho(1+2\varepsilon_1)V_{P0}^2 & c_{33} = \rho V_{P0}^2 \\
c_{44} = 0 & c_{55} = 0 & c_{66} = 0 \\
c_{12} = \rho V_{P0}^2(1+2\varepsilon_2)\sqrt{1+2\delta_3} & c_{13} = \rho V_{P0}^2\sqrt{1+2\delta_2} \\
c_{23} = \rho V_{P0}^2\sqrt{1+2\delta_1}
\end{cases}
$$

Accordingly, the corresponding Christoffel matrix is

$$
\begin{bmatrix}
c_{11}k_x^2 - \rho\omega^2 & c_{12}k_xk_y & c_{13}k_xk_z \\
c_{12}k_xk_y & c_{44}k_z^2 - \rho\omega^2 & c_{23}k_yk_z \\
c_{13}k_xk_z & c_{23}k_yk_z & c_{33}k_z^2 - \rho\omega^2
\end{bmatrix}
\qquad (9)
$$

Applying the Tsvankin notation to Eq. (9), the acoustic approximation of the P-wave dispersion relation can be expressed as

$$
\begin{aligned}
&\left(\rho\omega^2\right)^3 - \left(\rho(1+2\varepsilon_2)V_{P0}^2k_x^2 + \rho(1+2\varepsilon_1)V_{P0}^2k_y^2 + \rho V_{P0}^2k_z^2\right)\left(\rho\omega^2\right)^2 \\
&+ \rho^2(1+2\varepsilon_2)[(1+2\varepsilon_1)-(1+2\varepsilon_2)(1+2\delta_3)]V_{P0}^4k_x^2k_y^2\left(\rho\omega^2\right) \\
&+ \rho^2 2(\varepsilon_2-\delta_2)V_{P0}^4k_x^2k_z^2\left(\rho\omega^2\right) + \rho^2 2(\varepsilon_1-\delta_1)V_{P0}^4k_y^2k_z^2\left(\rho\omega^2\right) \\
&- \big[\rho^3(1+2\varepsilon_2)(1+2\varepsilon_1) + \rho^3 2(1+2\varepsilon_2)\sqrt{1+2\delta_3}\sqrt{1+2\delta_2} \\
&\quad \sqrt{1+2\delta_1} - (1+2\varepsilon_2)(1+2\delta_1) - (1+2\varepsilon_2)^2(1+2\delta_3) \\
&\quad - (1+2\varepsilon_1)(1+2\delta_2)\big]V_{P0}^6k_x^2k_y^2k_z^2 = 0
\end{aligned}
\qquad (10)
$$

Eq. (10) as well as being written as

Table 1
The time-consuming comparison between CPU and GPU.

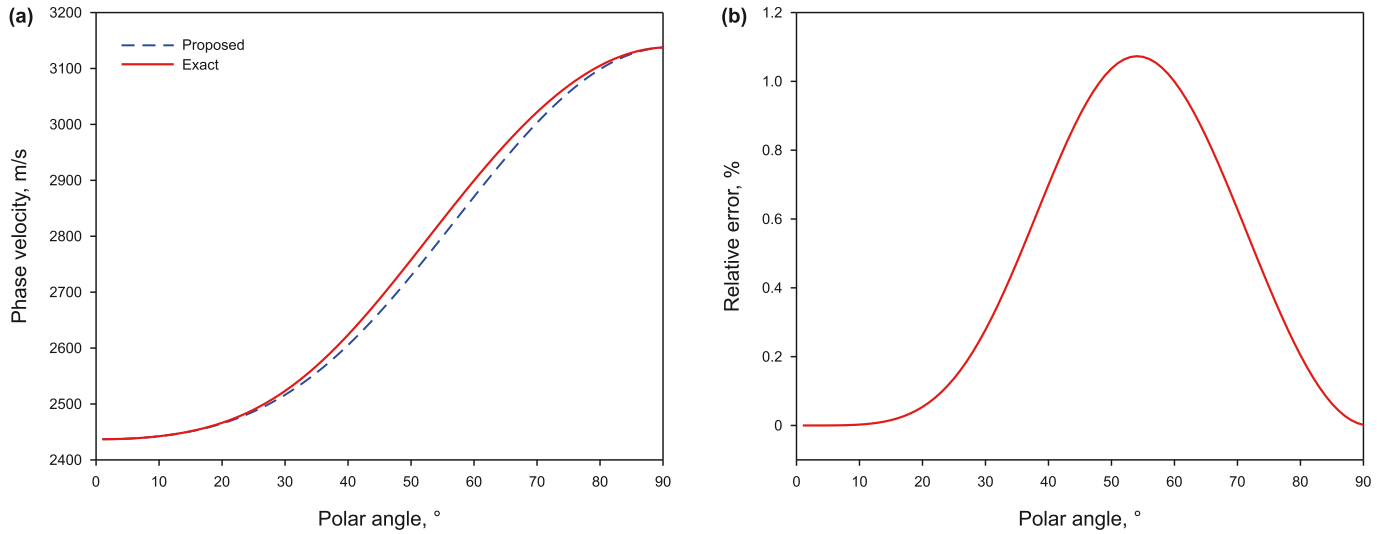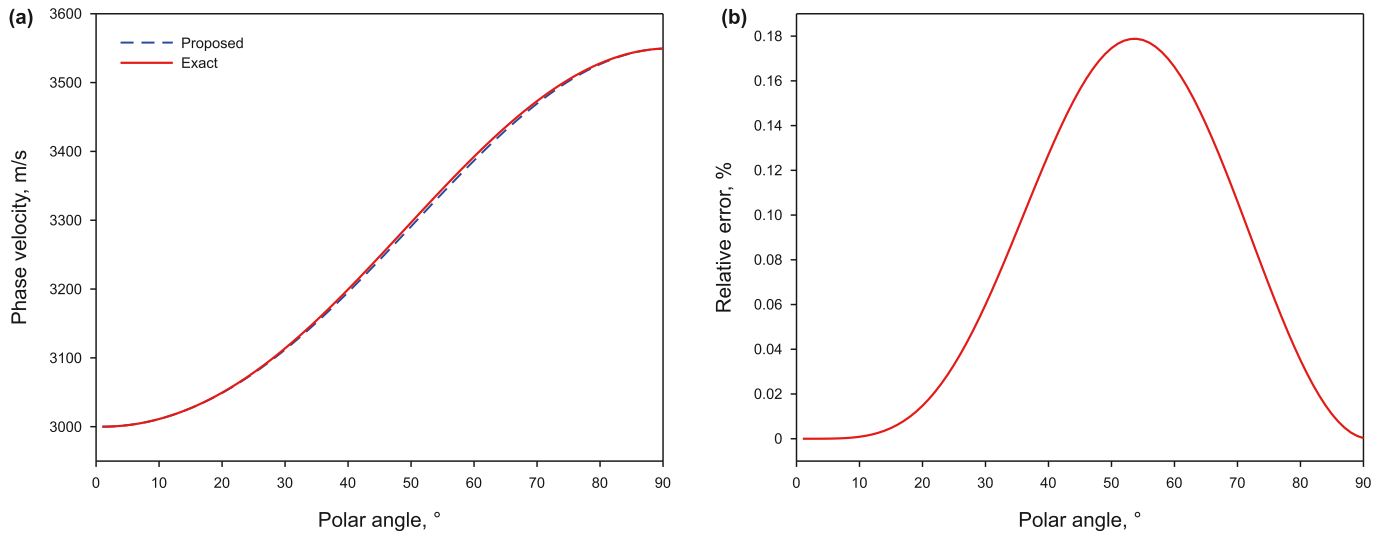| Model grid size	$100 \times 100 \times 100$	$200 \times 200 \times 200$	$300 \times 300 \times 300$
Time-consuming on CPU, s	118.34	1002.10	3418.95
Time-consuming on GPU, s	0.56	2.28	5.74
Speedup	215.16	439.52	595.64

(a)

(b)

Fig. 2. Phase velocity analysis between the proposed Eq. (12) (blue dashed curve) and the exact P-wave phase velocity (red solid curve) when the amplitude angle ϕ is 90°: **(a)** phase velocity; **(b)** relative error.

(a)

(b)

Fig. 3. Phase velocity analysis between the proposed Eq. (12) (blue dashed curve) and the exact P-wave phase velocity (red solid curve) when the amplitude angle ϕ is 90°: **(a)** phase velocity; **(b)** relative error.

$$\omega^2 = (1 + 2\varepsilon_2)V_{P0}^2 k_x^2 + (1 + 2\varepsilon_1)V_{P0}^2 k_y^2 + V_{P0}^2 k_z^2$$

$$- (1 + 2\varepsilon_2)[(1 + 2\varepsilon_1) - (1 + 2\varepsilon_2)(1 + 2\delta_3)]\frac{V_{P0}^4}{\omega^2}k_x^2 k_y^2$$

$$- 2(\varepsilon_2 - \delta_2)\frac{V_{P0}^4}{\omega^2}k_x^2 k_z^2 - 2(\varepsilon_1 - \delta_1)\frac{V_{P0}^4}{\omega^2}k_y^2 k_z^2$$

$$+ \Big[(1 + 2\varepsilon_2)(1 + 2\varepsilon_1) + 2(1 + 2\varepsilon_2)\sqrt{1 + 2\delta_3}\sqrt{1 + 2\delta_2}$$

$$\sqrt{1 + 2\delta_1}$$

$$+ (1 + 2\varepsilon_2)(1 + 2\delta_1) - (1 + 2\varepsilon_2)^2(1 + 2\delta_3)$$

$$- (1 + 2\varepsilon_1)(1 + 2\delta_2)\Big]\frac{V_{P0}^6}{\omega^4}k_x^2 k_y^2 k_z^2$$

(11)

Here, we set $V_{P0}^2/\omega^2 = 1/(k_x^2 + k_y^2 + k_z^2)$ and neglect higher-order terms, and then we get a new pure P-wave equation in the

frequency-wavenumber domain:

$$\omega^2 = (1 + 2\varepsilon_2)V_{P0}^2 k_x^2 + (1 + 2\varepsilon_1)V_{P0}^2 k_y^2 + V_{P0}^2 k_z^2$$

$$- 2(1 + 2\varepsilon_2)[\varepsilon_1 - \varepsilon_2 - \delta_3 - 2\varepsilon_2\delta_3]V_{P0}^2\frac{k_x^2 k_y^2}{k_x^2 + k_y^2 + k_z^2}$$

$$- 2(\varepsilon_2 - \delta_2)V_{P0}^2\frac{k_x^2 k_z^2}{k_x^2 + k_y^2 + k_z^2} - 2(\varepsilon_1 - \delta_1)V_{P0}^2\frac{k_y^2 k_z^2}{k_x^2 + k_y^2 + k_z^2}$$

(12)

Table 2
Anisotropic parameters for homogeneous media.

Model	ε_1	ε_2	δ_1	δ_2	δ_3
I	0.15	0.10	0.01	0.01	−0.01
II	0.20	−0.05	−0.1	−0.1	−0.1
III	0.30	0.20	−0.15	−0.15	−0.15
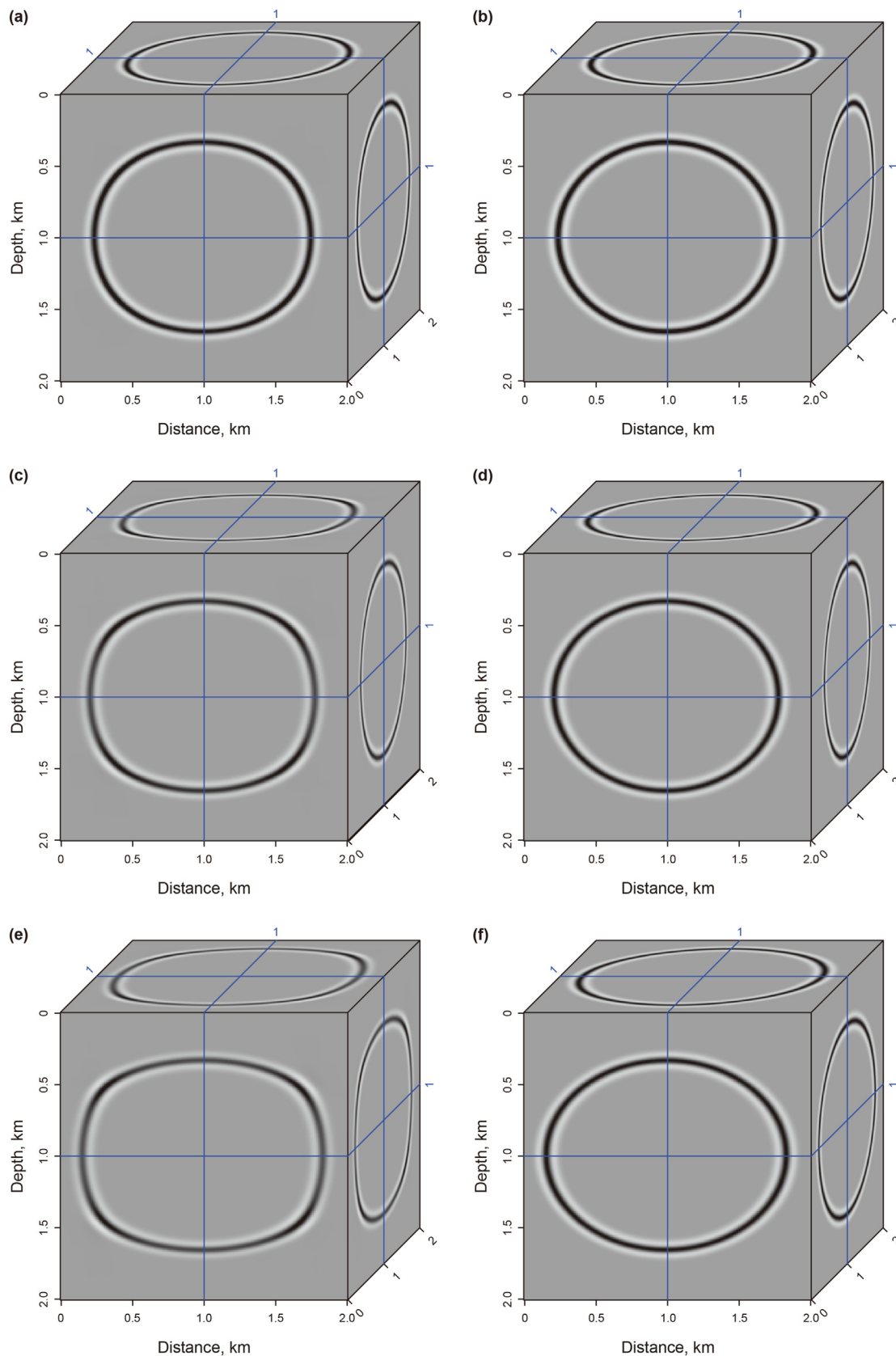
Fig. 4. Wavefield snapshots at 0.4 s in the 3D homogeneous media. **(a)**, **(c)** and **(e)** are the wavefields simulated by the proposed pure P-wave equation in the I, II and III models, respectively; **(b)**, **(d)** and **(f)** are the wavefields simulated by the elliptic approximation equation in I, II and III models, respectively.
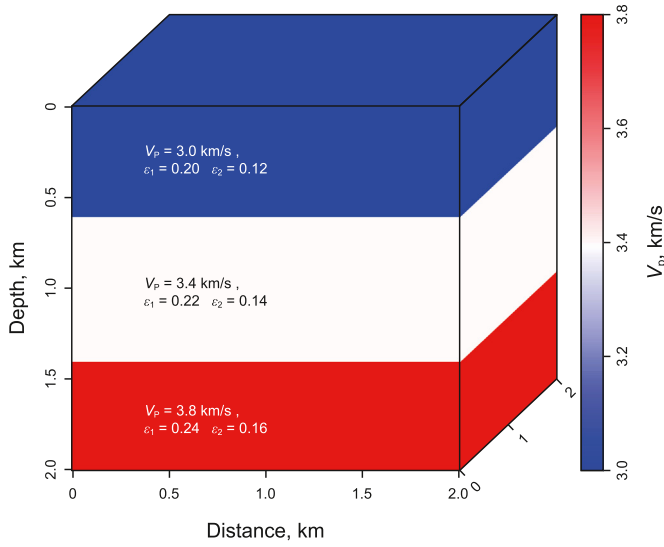
Fig. 5. Anisotropic parameters and velocity in a three-layer model.

In the time-space domain, according to the following relations and retaining the mixed wavenumber terms,

$$i\omega \leftrightarrow \frac{\partial}{\partial t} \quad ik_x \leftrightarrow \frac{\partial}{\partial x} \quad ik_y \leftrightarrow \frac{\partial}{\partial y} \quad ik_z \leftrightarrow \frac{\partial}{\partial z}$$

Eq. (12) can be transformed as

$$\frac{\partial^2 p}{\partial t^2} = (1+2\varepsilon_2)V_{P0}^2 \frac{\partial^2 p}{\partial x^2} + (1+2\varepsilon_1)V_{P0}^2 \frac{\partial^2 p}{\partial y^2} + V_{P0}^2 \frac{\partial^2 p}{\partial z^2}$$

$$-(1+2\varepsilon_2)2[\varepsilon_1 - \varepsilon_2 - \delta_3 - 2\varepsilon_2\delta_3]V_{P0}^2 \frac{k_x^2 k_y^2}{k_x^2 + k_y^2 + k_z^2}$$

$$-2(\varepsilon_2 - \delta_2)V_{P0}^2 \frac{k_x^2 k_z^2}{k_x^2 + k_y^2 + k_z^2} - 2(\varepsilon_1 - \delta_1)V_{P0}^2 \frac{k_y^2 k_z^2}{k_x^2 + k_y^2 + k_z^2}$$

$$(13)$$

where $p(x, y, z, t)$ is the pure P-wave wavefield in the time-space domain. In practice, the numerical solution of Eq. (13) is relatively simple and easy to implement. In this paper, a hybrid approach is used to implement numerical simulations of the derived new Eq. (13). The approach involves using the finite difference method to calculate for the spatial partial derivatives and the spectral method to calculate for the mixed partial derivatives to finally obtain the whole wavefield.

For elliptical anisotropy, that is, $\varepsilon_1 = \delta_1, \varepsilon_2 = \delta_2, \varepsilon_1 - \varepsilon_2 = (1 + 2\varepsilon_2)\delta_3$, in the wave-number domain, Eq. (13) can be reduced to

$$\omega^2 = (1+2\varepsilon_2)V_{P0}^2 k_x^2 + (1+2\varepsilon_1)V_{P0}^2 k_y^2 + V_{P0}^2 k_z^2 \qquad (14)$$

and in the time-space domain

$$\frac{\partial^2 p}{\partial t^2} = (1+2\varepsilon_2)V_{P0}^2 \frac{\partial^2 p}{\partial x^2} + (1+2\varepsilon_1)V_{P0}^2 \frac{\partial^2 p}{\partial y^2} + V_{P0}^2 \frac{\partial^2 p}{\partial z^2} \qquad (15)$$

3. Numerical examples

3.1. Efficiency and accuracy tests

In the numerical examples below, we have implemented the 3D
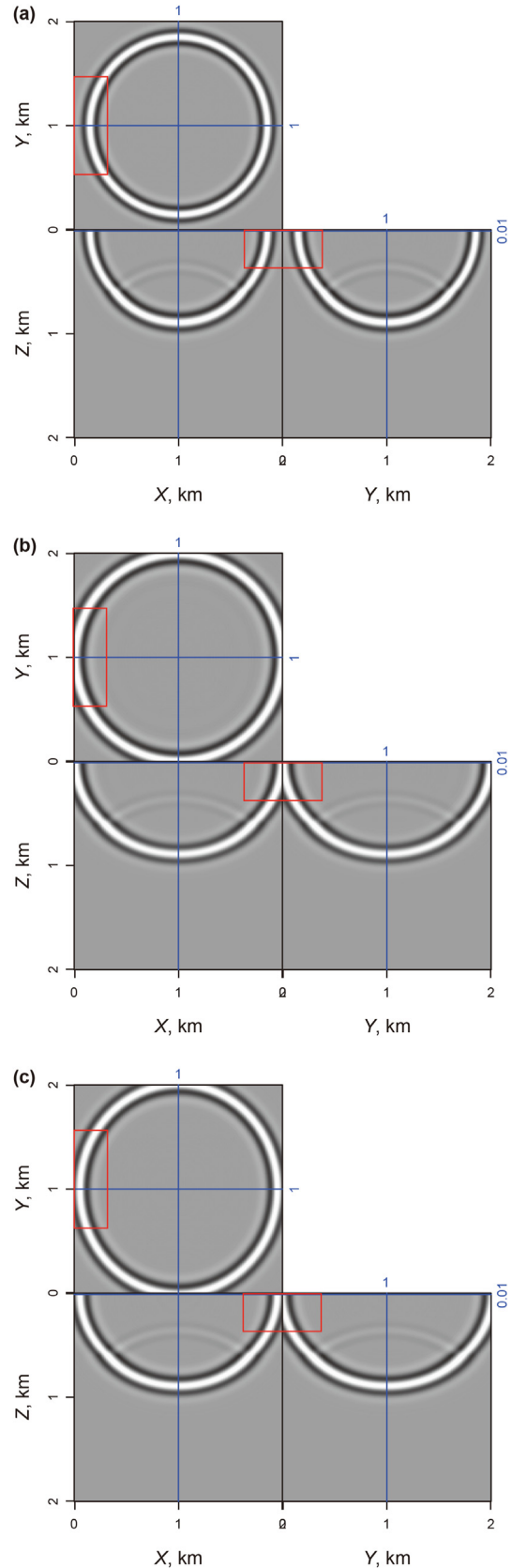
Fig. 6. Wavefields of the shot (located at (0.01 km, 1 km, 1 km)) in different media at 0.35 s in the 3D two-layer model. **(a)** ISO; **(b)** VTI; **(c)** ORT. The comparison at the blue line is shown in Fig. 7.
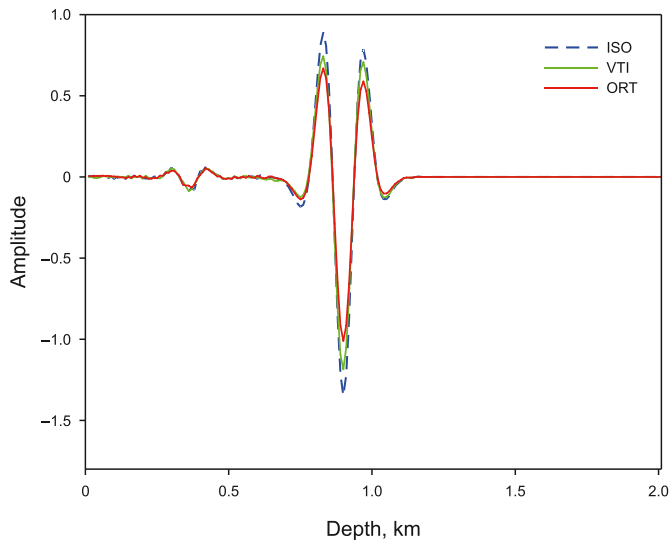
Fig. 7. The comparison of different media for single shot. The blue dashed line represents ISO media, the green solid line represents VTI media, and the red solid line represents ORT media.

forward modeling and RTM on the pure P-wave equation (Eq. (13) and (15)), using finite difference and pseudo-spectral methods. However, the conventional algorithm based on CPU for 3D computing requires enormous amounts of time. In dealing with massive data computing, GPU devices have higher performance than CPU devices because it has a large number of computing cores. Therefore, we apply GPU parallelization techniques in the algorithm steps to improve efficiency. First, to test the performance of GPU acceleration, we take three models of different sizes for acoustic modeling as examples. The device models of GPU are NVIDIA Quadro P5000, which has 16 GB GDDR5X memory and 2560 processors. The CPU model name is Inter Xeon Silver 4214, which running at 2.20 GHz with 256 GB RAM memory. The time-consuming comparison between CPU and GPU can be seen in Table 1. As observed, as the model size increases, the CPU time consumption increases faster than the GPU. Therefore, with GPU acceleration in 3D computation can reduce a large amount of time and significantly improve computational efficiency.

Second, in order to verify the accuracy of the proposed equation, we test two models in Figs. 2 and 3. In Fig. 2, the model is taken from Schoenberg (1997), and the model parameters are $V_P = 2.437$ km/s, $\varepsilon_1 = 0.329$, $\varepsilon_2 = 0.258$, $\delta_1 = 0.083$, $\delta_2 = -0.078$, $\delta_3 = -0.106$, $\gamma_1 = 0.182$, $\gamma_2 = 0.0455$, $V_s = 1.265$ km/s. The variation of γ_1, γ_2 and V_s have no influence on P-wave velocity. Fig. 2 shows the error between Eq. (12) and the exact phase velocity for orthorhombic media. The relative error in Fig. 2(b) becomes zero when the polar angle θ in $0–30°$ and $90°$, and relatively minor error begins to appear from $30°$. Fig. 3 shows the relative error under the strong anisotropic model, and the model parameters are $V_P = 3$ km/s, $\varepsilon_1 = 0.2$, $\varepsilon_2 = 0.6$, $\delta_1 = 0.15$, $\delta_2 = -0.15$, $\delta_3 = -0.2$. The characteristics of the relative error in Fig. 3 are the same as in Fig. 2, but the order of magnitude is 10 times smaller than that in Fig. 2, and the phase velocity curve matches perfectly with the exact P-wave phase velocity.

Next, we performed the numerical simulation of the pure P-wave equation under several different sets of Thomsen's

anisotropic parameter models in Table 2. Fig. 4 is the wavefield snapshots at 0.4 s in several 3D homogeneous ORT models. The main frequency of 20Hz ricker-wavelet is set as the source in the center of the model with the size of 2 km × 2 km × 2 km. The vertical P-wave velocity is set to $V_P = 2.2$ km/s, and the time and space sampling intervals are set to 1 ms and 0.01 km respectively to satisfy the stability and dispersion conditions. Fig. 4(a), (c), and (e) show the wavefields simulated by Eq. (13) in I, II, III models, respectively; Fig. 4(b), (d), and (f) show the wavefields simulated by Eq. (15) in I, II, III models, respectively. Both figures show that the wavefields have only P wave components, without any presence of shear wave artifacts.

3.2. 3D RTM tests

Finally, we tested the RTM results of the two models. Fig. 5 shows a simple three-layer model for 3D homogeneous medium. The model size is 2 km × 2 km × 2 km, and Ricker-wavelet (the main frequency is set to 25Hz) is set as the source at a depth of 0.01 km near the surface. A total of 100 shots are set, with 10 shots in each row and column. The time and space steps are 1 ms and 0.01 km, respectively. The thickness of the first layer is 0.6 km and the model parameters are $V_P = 3$ km/s, $\varepsilon_1 = 0.2$, $\varepsilon_2 = 0.12$. The middle layer is 0.8 km, and $V_P = 3.4$ km/s, $\varepsilon_1 = 0.22$, $\varepsilon_2 = 0.14$. And the bottom layer is 0.6 km, $V_P = 3.8$ km/s, $\varepsilon_1 = 0.24$, $\varepsilon_2 = 0.16$. Fig. 6 displays the wavefield snapshots of three media at 0.35 s, and we extract the waveform slices at the position (0.01 km, 1 km, 1 km) of the blue line which is shown in Fig. 7. In order to better compare the imaging results of different media methods, we extracted the red frame part in Fig. 8(a), (c), (e), and enlarged it to show in Fig. 8(b), (d), (f), respectively. As observed in Fig. 8(c) and (e), the imaging results of VTI and ORT media in the figure are accurate for a simple three-layer model, all of which can accurately represent the structure of the model, with a slight difference in low-frequency noise and amplitude. However, the imaging result of ISO media is poor, and there are obvious imaging artifacts at both reflection interfaces. In particular, the first layer of reflection interface cannot be accurately positioned.

The last example is the modified SEG/EAGE 3D salt model. Fig. 9 depicts the vertical P-wave velocity (Fig. 9(a)), and the anisotropic parameters ε_1 and ε_2 (Fig. 9(b) and (c)). The model size is 3.38 km × 3.38 km × 2 km, and the space difference intervals used are 0.01 km × 0.01 km × 0.01 km. The time sampling step is 1 ms. Ricker-wavelet (the main frequency is set to 15 Hz) is set as the source at a depth of 0.01 km near the surface. A total of 256 shots are set, with 16 shots in each row and column. For comparison, we tested in isotropic (ISO), VTI, and ORT media. And Fig. 10(a)–(c) show the RTM results of the acoustic equation, VTI and ORT decoupled P-wave equation, respectively.

As observed, in ORT media, the imaging of salt structure is clearer and better than in other media, and some deep structure imaging is also clearer by using the equation derived in this paper for RTM. This is further demonstrated in Fig. 11, where Fig. 11(a), (c) and (e) show the zoomed views of the red boxes in Fig. 10(a)–(c), respectively; Fig. 11(b), (d) and (f) show the zoomed view of the yellow boxes in Fig. 10(a)–(c), respectively.

4. Discussions

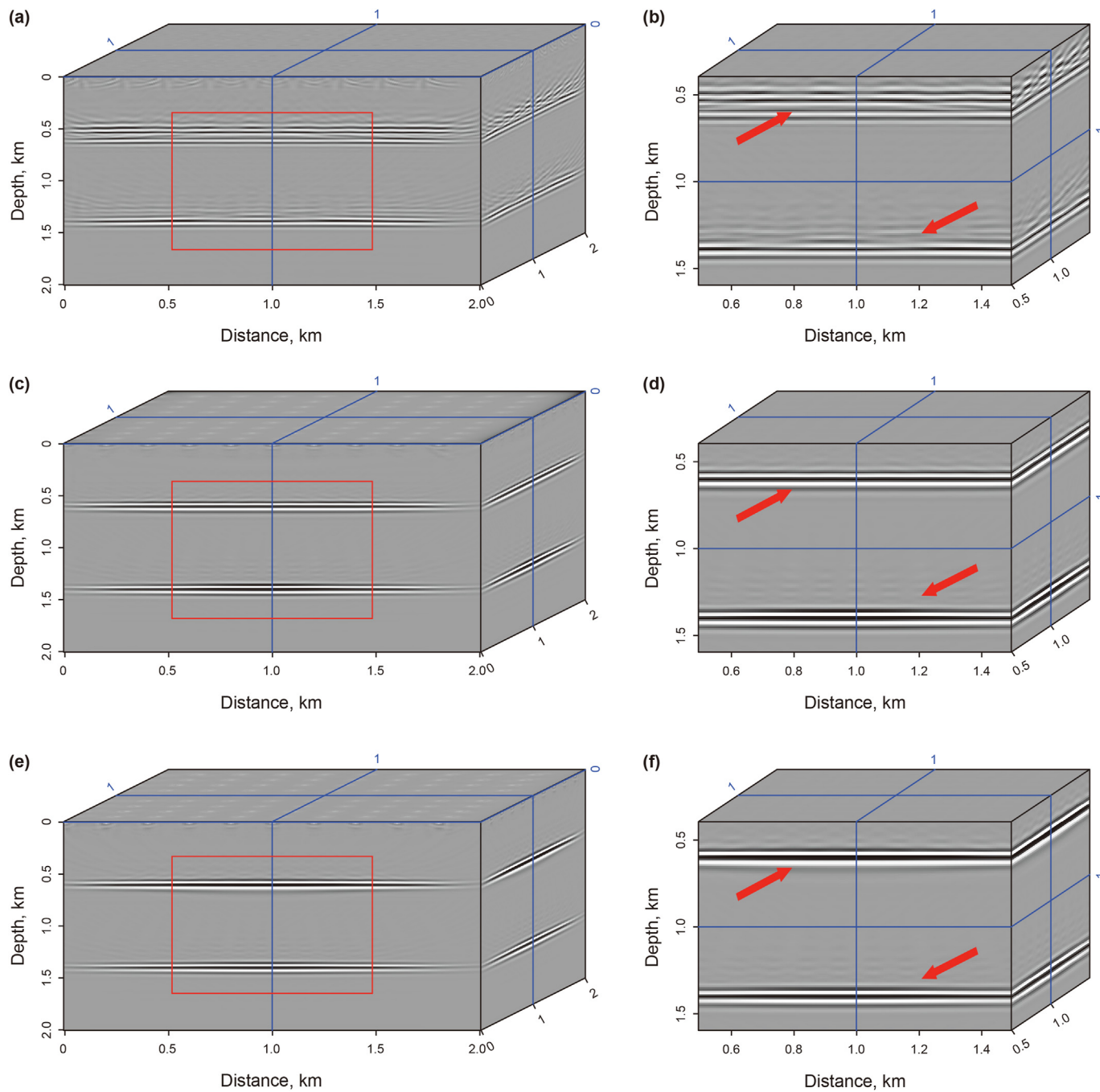When compared to 2D computation, 3D forward modeling and

Fig. 8. The comparison of migration results using different media from 100 shots. **(a)** ISO RTM; **(b)** red frame part in Fig. 8(a); **(c)** VTI RTM; **(d)** red frame part in Fig. 8c; **(e)** ORT RTM; **(f)** red frame part in Fig. 8(e).
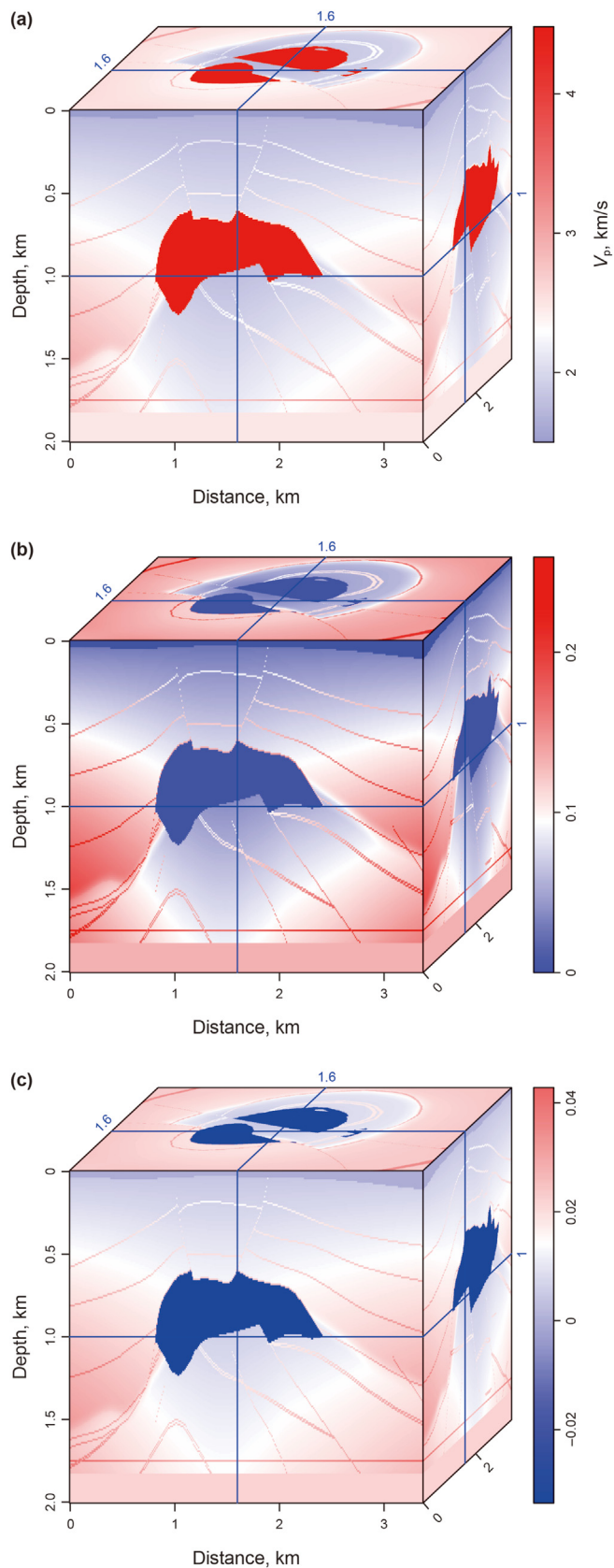
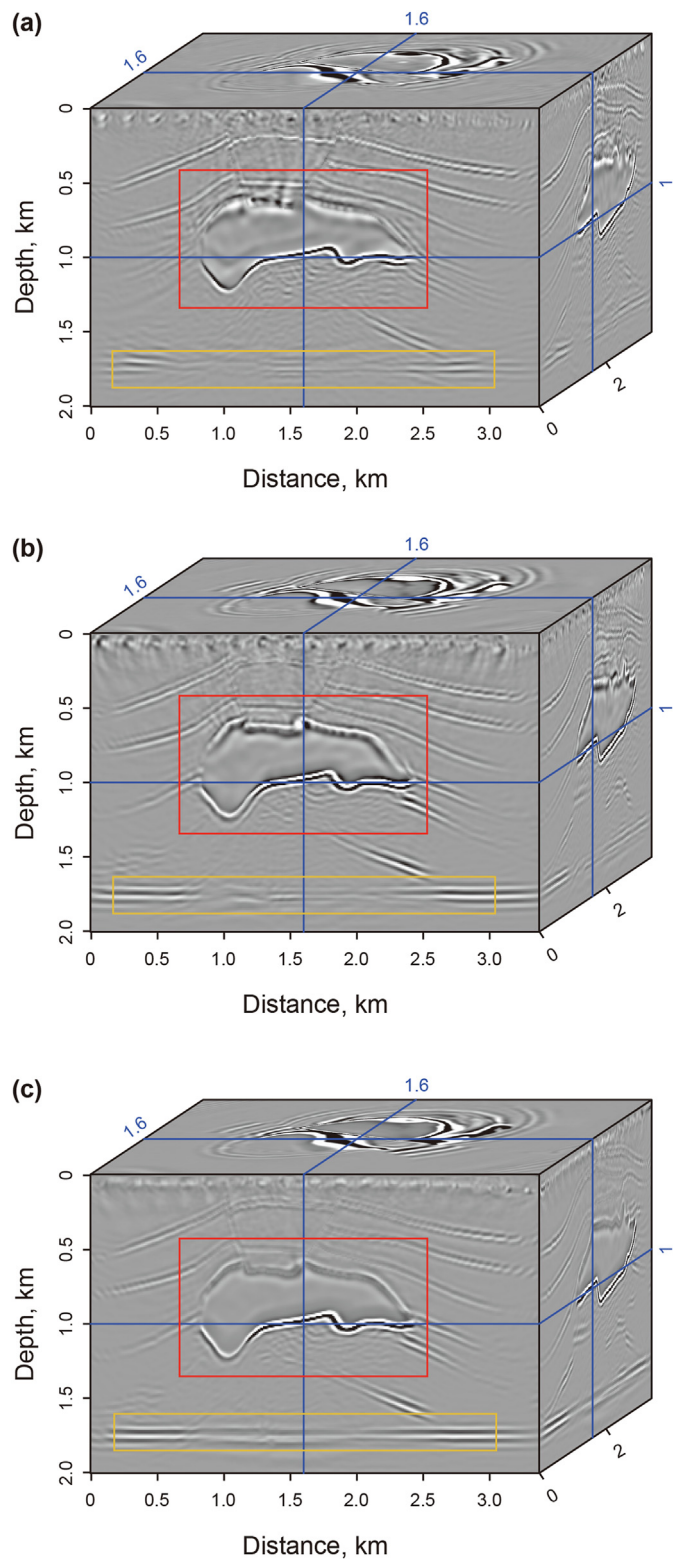**Fig. 9.** SEG/EAGE 3D salt models. **(a)** vertical P-wave velocity; **(b)** ε_1; **(c)** ε_2.

Fig. 10. The comparison of migration results using different media from 256 shots. **(a)** ISO RTM; **(b)** VTI RTM; **(c)** ORT RTM.
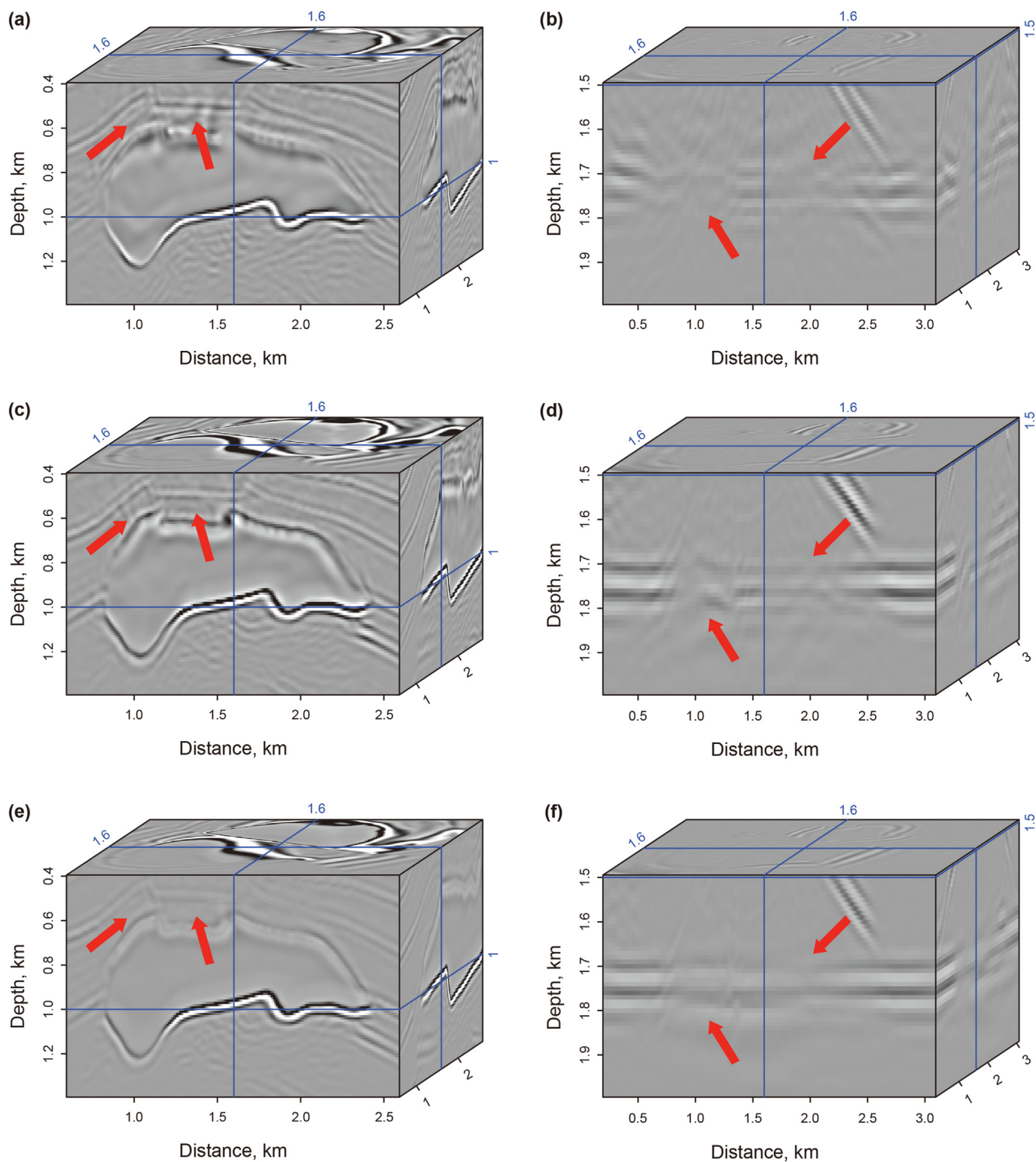
Fig. 11. Zoom view of RTM results in Fig. 10. **(a)** ISO RTM imaging result of the red frame in Fig. 10(a); **(b)** ISO RTM imaging result of the yellow frame in Fig. 10(a); **(c)** VTI RTM imaging result of the red frame in Fig. 10(b); **(d)** VTI RTM imaging result of the yellow frame in Fig. 10(b); **(e)** ORT RTM imaging result of the red frame in Fig. 10(c); **(f)** ORT RTM imaging result of the yellow frame in Fig. 10(c).

reverse time migration can provide more subsurface geological information, and the result in seismic imaging is clearer with higher resolution. However, 3D data volume and its computational cost can be substantial. In this paper, we design and implement a 3D RTM algorithm based on GPU, which greatly reduces the computational cost. However, the model sizes used in the numerical examples of this paper are relatively small, so the storage and calculation burden are not prohibitive. This remains a challenge for future applications to the 3D field data.

The exact dispersion relation of the orthorhombic medium is extremely complex, which can be computationally intensive for modeling or migration. The approximate methods and mathematical transformations used in the derivation of the new pure P-wave equation inevitably reduce the accuracy, but significantly improve the efficiency of the solution. The new pure P-wave equation requires the use of the pseudo-spectral method, specifically, 3D FFT, which undoubtedly increases the calculation time compared to the equation that only needs to be solved by the finite difference method. Generally, this method is more straightforward than the previous exact phase velocity formula.

5. Conclusions

We have derived a novel pure P-wave equation for orthorhombic media with elliptic and anelliptic terms starting from the Christoffel equation. To reduce computational costs, we used a hybrid method of finite-difference and pseudo-spectral methods to optimize the algorithm by reducing the number of 3D Fourier transforms to implement modeling. In addition, we implemented 3D RTM by using the simplified equations of the elliptic approximation. Numerical examples show that the use of pure P-wave equation in forward modeling and RTM can avoid shear wave artifacts and remain stable even when anisotropic parameters vary significantly, it can also obtain accurate image results while improving efficiency.

CRediT authorship contribution statement

Ying-Hui Liu: Writing − original draft, Writing − review & editing, Data curation, Investigation, Visualization. **Jian-Ping Huang:** Funding acquisition, Project administration, Resources, Supervision, Writing − review & editing. **Liang Chen:** Writing − review & editing. **Qiang Mao:** Writing − review & editing. **Kun Tian:** Funding acquisition.

Declaration of competing interest

The authors declare that they have no known competing financial interests or personal relationships that could have appeared to influence the work reported in this paper.

Acknowledgments

Appendix A

Solving for the eigenvalues in Eq. (6) yields the following cubic equation for the phase velocity valid for ORT media

$$x^3 + Ax^2 + Bx + C = 0 \tag{A-1}$$

where $x = \rho\omega^2$ and

$$
\begin{aligned}
A &= -\left(c_{11}k_x^2 + c_{66}k_y^2 + c_{55}k_z^2\right) - \left(c_{66}k_x^2 + c_{22}k_y^2 + c_{44}k_z^2\right) \\
&\quad - \left(c_{55}k_x^2 + c_{44}k_y^2 + c_{33}k_z^2\right) \\
B &= \left(c_{11}k_x^2 + c_{66}k_y^2 + c_{55}k_z^2\right)\left(c_{55}k_x^2 + c_{44}k_y^2 + c_{33}k_z^2\right) \\
&\quad + \left(c_{66}k_x^2 + c_{22}k_y^2 + c_{44}k_z^2\right)\left(c_{55}k_x^2 + c_{44}k_y^2 + c_{33}k_z^2\right) \\
&\quad + \left(c_{66}k_x^2 + c_{22}k_y^2 + c_{44}k_z^2\right)\left(c_{11}k_x^2 + c_{66}k_y^2 + c_{55}k_z^2\right) \\
&\quad - (c_{23}+c_{44})^2 k_y^2 k_z^2 - (c_{13}+c_{55})^2 k_x^2 k_z^2 - (c_{12}+c_{66})^2 k_x^2 k_y^2 \\
C &= -\left(c_{11}k_x^2 + c_{66}k_y^2 + c_{55}k_z^2\right)\left(c_{66}k_x^2 + c_{22}k_y^2 + c_{44}k_z^2\right) \\
&\quad \left(c_{55}k_x^2 + c_{44}k_y^2 + c_{33}k_z^2\right) \\
&\quad - 2(c_{12}+c_{66})k_x k_y (c_{13}+c_{55})k_x k_z (c_{23}+c_{44})k_y k_z \\
&\quad + \left(c_{11}k_x^2 + c_{66}k_y^2 + c_{55}k_z^2\right)(c_{23}+c_{44})^2 k_y^2 k_z^2 \\
&\quad + \left(c_{66}k_x^2 + c_{22}k_y^2 + c_{44}k_z^2\right)(c_{13}+c_{55})^2 k_x^2 k_z^2 \\
&\quad + \left(c_{55}k_x^2 + c_{44}k_y^2 + c_{33}k_z^2\right)(c_{12}+c_{66})^2 k_x^2 k_y^2
\end{aligned} \tag{A-2}
$$

Introduction of a variable $y = x + A/3$, Eq. (A−1) eliminates the squared term and becomes (Tsvankin, 1997)

$$y^3 + Dy + E = 0 \tag{A-3}$$

and the coefficients

$$D = -\frac{A^2}{3} + B \tag{A-4}$$

$$E = 2\left(\frac{A}{3}\right)^3 - \frac{AB}{3} + C \tag{A-5}$$

Due to the fact that the Christoffel matrix is real and symmetric, the coefficients D are negative and in order for the roots of Eq. (A−3) to be real, a condition needs to be satisfied for the coefficients D and E:

$$\Delta = \left(\frac{D}{3}\right)^3 + \left(\frac{E}{2}\right)^2 \leq 0 \tag{A-6}$$

There have three solutions to Eq. (A−3) and can be expressed as

$$y_{1,2,3} = 2\sqrt{\frac{-D}{3}}\cos\left(\frac{\beta}{3} + k\frac{2\pi}{3}\right), \qquad k = 0, 1, 2 \tag{A-7}$$

where $\cos\beta = -\dfrac{E}{2\sqrt{(-D/3)^3}}$, $0 \leq \beta \leq \pi$.

Combined with $x = \rho\omega^2 = y - A/3$, a representation of phase velocity in orthorhombic media can be obtained

$$\omega^2 = \frac{1}{\rho}\left[2\sqrt{\frac{-D}{3}}\cos\left(\frac{\beta}{3}+k\frac{2\pi}{3}\right) - A\bigg/3\right], \qquad k = 0,1,2 \tag{A-8}$$

Appendix B

In the P-wave exact phase velocity (Eq. (A–8) when $k = 0$) of orthorhombic media, the cosine function can be expressed as Eq. (B–1) after Taylor expansion,

$$\cos\left(\frac{\beta}{3}\right) \approx 1 - \frac{\beta^2}{18} + \frac{1}{4!}\frac{\beta^4}{81} - \cdots \tag{B-1}$$

For isotropic, $\beta = 0$, so that in the case of weak anisotropic $\cos\left(\frac{\beta}{3}\right) \approx 1$, and Eq. (A–8) reduces to

$$\omega^2 = \frac{1}{\rho}\left(2\sqrt{\frac{-D}{3}} - A\bigg/3\right) \tag{B-2}$$

According to Eq. (A–2), $-D$ can be expressed as

and Eq. (B–3) can be further reduced to

$$-D = \frac{1}{3}\rho^2\left[\left(V_{P0}^2 - V_{S0}^2\right)^2 + L\left(V_{P0}^2 - V_{S0}^2\right)\right]^2 \tag{B-4}$$

where

$$L = L_1 k_x^4 + L_2 k_y^4 + L_3 k_z^4 + L_4 k_x^2 k_y^2 + L_5 k_x^2 k_z^2 + L_6 k_y^2 k_z^2 \tag{B-5}$$

$$
\begin{aligned}
L_1 &= 4\varepsilon_2 V_{P0}^2 - 2\gamma_1 V_{S0}^2 \\
L_2 &= 4\varepsilon_1 V_{P0}^2 - 2\left(\gamma_1 + \frac{\gamma_1 - \gamma_2}{1 + 2\gamma_2}\right)V_{S0}^2 \\
L_3 &= -2\gamma_s V_{S0}^2 \\
L_4 &= 2(5\varepsilon_2 - \varepsilon_1 + 3\delta_3)V_{P0}^2 - 2\left(2\gamma_1 + \frac{\gamma_1 - \gamma_2}{1 + 2\gamma_2}\right)V_{S0}^2 \\
L_5 &= 2(-\varepsilon_2 + 3\delta_2)V_{P0}^2 - 2\left(\gamma_1 + \frac{\gamma_1 - \gamma_2}{1 + 2\gamma_2}\right)V_{S0}^2 \\
L_6 &= 2(-\varepsilon_1 + 3\delta_1)V_{P0}^2 - 2\left(\gamma_1 + 2\frac{\gamma_1 - \gamma_2}{1 + 2\gamma_2}\right)V_{S0}^2
\end{aligned} \tag{B-6}
$$

where, $\gamma_s = \frac{\gamma_1 - \gamma_2}{1 + 2\gamma_2}$.

Then, taking the mathematic transformation of Eq. (B–4), we can obtain

$$
\begin{aligned}
-D ={}& \frac{1}{3}\rho^2\left[(1 + 2\varepsilon_2)V_{P0}^2 k_x^2 + (1 + 2\gamma_1)V_{S0}^2 k_y^2 + V_{S0}^2 k_z^2\right]^2 \\
&+ \frac{1}{3}\rho^2\left[(1 + 2\gamma_1)V_{S0}^2 k_x^2 + (1 + 2\varepsilon_1)V_{P0}^2 k_y^2 + [(1 + 2\gamma_1)/(1 + 2\gamma_2)]V_{S0}^2 k_z^2\right]^2 \\
&+ \frac{1}{3}\rho^2\left[V_{S0}^2 k_x^2 + [(1 + 2\gamma_1)/(1 + 2\gamma_2)]V_{S0}^2 k_y^2 + V_{P0}^2 k_z^2\right]^2 \\
&- \frac{1}{3}\rho^2\left[(1 + 2\varepsilon_2)V_{P0}^2 k_x^2 + (1 + 2\gamma_1)V_{S0}^2 k_y^2 + V_{S0}^2 k_z^2\right] \\
&\left[(1 + 2\gamma_1)V_{S0}^2 k_x^2 + (1 + 2\varepsilon_1)V_{P0}^2 k_y^2 + [(1 + 2\gamma_1)/(1 + 2\gamma_2)]V_{S0}^2 k_z^2\right] - \frac{1}{3}\rho^2\left[(1 + 2\varepsilon_2)V_{P0}^2 k_x^2 + (1 + 2\gamma_1)V_{S0}^2 k_y^2 + V_{S0}^2 k_z^2\right] \\
&\left[V_{S0}^2 k_x^2 + [(1 + 2\gamma_1)/(1 + 2\gamma_2)]V_{S0}^2 k_y^2 + V_{P0}^2 k_z^2\right] - \frac{1}{3}\rho^2\left[(1 + 2\gamma_1)V_{S0}^2 k_x^2 + (1 + 2\varepsilon_1)V_{P0}^2 k_y^2 + [(1 + 2\gamma_1)/(1 + 2\gamma_2)]V_{S0}^2 k_z^2\right]\cdot \\
&\left[V_{S0}^2 k_x^2 + [(1 + 2\gamma_1)/(1 + 2\gamma_2)]V_{S0}^2 k_y^2 + V_{P0}^2 k_z^2\right] + \rho^2\left[(1 + 2\varepsilon_2)V_{P0}^2 k_x k_y\left(1 - V_{S0}^2(1 + 2\gamma_1)\bigg/V_{P0}^2(1 + 2\varepsilon_2)\right) + \rho^2 \right. \\
&\left[V_{P0}^2 k_y k_z\left(1 - V_{S0}^2(1 + 2\gamma_1)\bigg/V_{P0}^2(1 + 2\gamma_2)\right)\right. \\
&\left.\sqrt{1 + 2\delta_3\bigg/\left(1 - V_{S0}^2(1 + 2\gamma_1)\bigg/V_{P0}^2(1 + 2\varepsilon_2)\right)}\right]^2 \\
&+ \rho^2\left[V_{P0}^2 k_x k_z\left(1 - V_{S0}^2\bigg/V_{P0}^2\right)\sqrt{1 + 2\delta_2\bigg/\left(1 - V_{S0}^2\bigg/V_{P0}^2\right)}\right]^2 \\
&\left.\sqrt{1 + 2\delta_1\bigg/\left(1 - V_{S0}^2(1 + 2\gamma_1)\bigg/V_{P0}^2(1 + 2\gamma_2)\right)}\right]^2
\end{aligned} \tag{B-3}
$$

$$\sqrt{\frac{-D}{3}} = \frac{1}{3}\rho\left[\left(V_{P0}^2 - V_{S0}^2\right) + \frac{L}{2}\right] \tag{B-7}$$

Furthermore, according to Eq. (A-2), $-A$ can be expressed as

$$-A = \rho\left[V_{P0}^2 + 2V_{S0}^2 + 2\left(\varepsilon_2 V_{P0}^2 + \gamma_1 V_{S0}^2\right)k_x^2\right.$$
$$\left. + 2\left(\varepsilon_1 V_{P0}^2 + \left(\gamma_1 + \frac{\gamma_1 - \gamma_2}{1 + 2\gamma_2}\right)V_{S0}^2\right)k_y^2 + 2\frac{\gamma_1 - \gamma_2}{1 + 2\gamma_2}V_{S0}^2 k_z^2\right] \tag{B-8}$$

Combining Eq. (B–7) and (B–8) into Eq. (B–2), we can finally get the expression for the weak-anisotropy approximation of the phase velocity of the P-wave.

$$V^2 = V_{P0}^2\left[1 + 2\varepsilon_2 k_x^4 + 2\varepsilon_1 k_y^4 + 2\delta_2 k_x^2 k_z^2 + 2\delta_1 k_y^2 k_z^2 + 2(2\varepsilon_2 + \delta_3)k_x^2 k_y^2\right] \tag{B-9}$$

According to the following relationship,

$$k_x = \sin\theta\cos\phi, k_y = \sin\theta\sin\phi, k_z = \cos\theta$$

Eq. (B–9) can also be written as

$$V^2 = V_{P0}^2[1 + 2\varepsilon_2\sin^4\theta\cos^4\phi + 2\varepsilon_1\sin^4\theta\sin^4\phi + 2\delta_2\sin^2\theta\cos^2\phi\cos^2\theta$$
$$+ 2\delta_1\sin^2\theta\sin^2\phi\cos^2\theta + 2(2\varepsilon_2 + \delta_3)\sin^4\theta\cos^2\phi\sin^2\phi] \tag{B-10}$$

References

Alkhalifah, T., 1998. Acoustic approximations for processing in transversely isotropic media. Geophysics 63 (2), P623–P631. https://doi.org/10.1190/1.1444361.

Alkhalifah, T., 2000. An acoustic wave equation for anisotropic media. Geophysics 65 (4), 1239–1250. https://doi.org/10.1190/1.1444815.

Alkhalifah, T., 2003. An acoustic wave equation for orthorhombic anisotropy. Geophysics 68 (4), 1169–1172. https://doi.org/10.1190/1.1598109.

Abedi, M.M., Stovas, A., 2020. A new acoustic assumption for orthorhombic media. Geophys. J. Int. 223 (2), 1118–1129. https://doi.org/10.1093/gji/ggaa367.

Bush, I., Crampin, S., 1991. Paris Basin VSPs: case history establishing combinations of fine-layer (or lithologic) anisotropy and crack anisotropy from modeling shear wavefields near point singularities. Geophys. J. Int. 107 (3), 433–447. https://doi.org/10.1111/j.1365-246X.1991.tb01405.x.

Cheng, J., Kang, W., 2014. Simulating propagation of separated wave modes in general anisotropic media, Part I: qP-wave propagators. Geophysics 79 (1), C1–C18. https://doi.org/10.1190/geo2012-0504.1.

Crampin, S., Evans, R., Atkinson, B.K., 1984. Earthquake prediction: a new physical basis. Geophys. J. Int. 76 (1), 147–156. https://doi.org/10.1111/j.1365-246X.1984.tb05030.x.

Du, Q.Z., 2004. Wavefield forward modeling with the pseudo-spectral method in viscoelastic and azimuthally anisotropic media. Acta Phys. Sin. 53 (12), 4428–4434. https://doi.org/10.7498/aps.53.4428.

Du, Q.Z., Guo, C.F., Gong, X.F., 2015. Hybrid PS/FD numerical simulation and stability analysis of pure P-wave propagation in VTI media. Chin. J. Geophys. 58 (4), 1290–1304. https://doi.org/10.6038/cjg20150417.

Du, X., Fletcher, R.P., Fowler, P.J., 2008. A new pseudo-acoustic wave equation for VTI media. In: 70th EAGE Conference and Exhibition Incorporating SPE EUROPEC, Expanded Abstracts. https://doi.org/10.3997/2214-4609.20147774 cp–40.

Duveneck, E., Milcik, P., Bakker, P.M., et al., 2008. Acoustic VTI wave equations and their application for anisotropic reverse-time migration. In: 78th Annual International Meeting. SEG Expanded Abstracts, pp. 2186–2190. https://doi.org/10.1190/1.3059320.

Duveneck, E., Bakker, P.M., 2011. Stable P-wave modeling for reverse-time migration in tilted TI media. Geophysics 76 (2), S65–S75. https://doi.org/10.1190/1.3533964.

Fletcher, R.P., Du, X., Fowler, P.J., 2009. Reverse time migration in tilted transversely isotropic (TTI) media. Geophysics 74 (6), WCA179–WCA187. https://doi.org/10.1190/1.3269902.

Fowler, P.J., Du, X., Fletcher, R.P., 2010. Coupled equations for reverse time migration in transversely isotropic media. Geophysics 75 (1), S11–S22. https://doi.org/10.1190/1.3294572.

Fowler, P.J., King, R., 2011. Modeling and reverse time migration of orthorhombic pseudo-acoustic P-waves. In: 81th Annual International Meeting, SEG Expanded Abstracts, pp. 190–195. https://doi.org/10.1190/1.3627580.

Guan, H., Dussaud, E., Denel, B., Williamson, P., 2011. Techniques for an efficient implementation of RTM in TTI media. In: 81th Annual International Meeting. SEG Expanded Abstracts, pp. 3193–3197. https://doi.org/10.1190/1.3627902.

Huang, J.Q., Li, Z.C., 2017. Modeling and reverse time migration of pure quasi-P-waves in complex TI media with a low-rank decomposition. Chin. J. Geophys. 60 (2), 704–721. https://doi.org/10.6038/cjg20170223 (in Chinese).

Liu, F., Morton, S.A., Jiang, S., et al., 2009. Decoupled wave equations for P and SV waves in an acoustic VTI media. In: 79th Annual International Meeting, SEG Expanded Abstracts, pp. 2844–2848. https://doi.org/10.1190/1.3255440.

Mu, X., Huang, J., Guo, X., et al., 2019. Least-squares reverse time migration based on pure qP-wave equation in TTI media. In: 89th Annual International Meeting. SEG Expanded Abstracts, pp. 4256–4260. https://doi.org/10.1190/segam2019-3203604.1.

Mu, X., Huang, J., Yong, P., et al., 2020a. Modeling of pure qP- and qSV-waves in tilted transversely isotropic media with the optimal quadratic approximation. Geophysics 85 (2), C71–C89. https://doi.org/10.1190/geo2018-0460.1.

Mu, X., Huang, J., Yang, J., et al., 2020b. Least-squares reverse time migration in TTI media using a pure P-wave equation. Geophysics 85 (4), S199–S216. https://doi.org/10.1190/geo2019-0320.1.

Postma, G.W., 1955. Wave propagation in a stratified medium. Geophysics 20 (4), 780–806. https://doi.org/10.1190/1.1438187.

Stovas, A., Masmoudi, N., Alkhalifah, T., 2016. Application of perturbation theory for P-wave eikonal equation in orthorhombic media. Geophysics 81 (6), C309–C317. https://doi.org/10.1190/geo2016-0097.1.

Stovas, A., Alkhalifah, T., bin Waheed, U., 2020. Pure P and S wave equations in transversely isotropic media. Geophys. Prospect. 68 (9), 2762–2769. https://doi.org/10.1111/1365-2478.13026.

Stovas, A., Roganov, Y., Roganov, V., 2021a. Wave characteristics in elliptical orthorhombic media. Geophysics 86 (3), C89–C99. https://doi.org/10.1190/geo2020-0509.1.

Stovas, A., Roganov, Y., Roganov, V., 2021b. Perturbation of phase velocities in elastic orthorhombic media. Geophysics 86 (4), C101–C118. https://doi.org/10.1190/geo2020-0820.1.

Stovas, A., Roganov, Y., Roganov, V., 2021c. Pure mode P and S wave phase velocity equations in elastic orthorhombic media. Geophysics 86 (5), C143–C156. https://doi.org/10.1190/geo2021-0067.1.

Thomsen, L., 1986. Weak elastic anisotropy. Geophysics 51 (10), 1954–1966.

Tsvankin, I., 1997. Anisotropic parameters and P-wave velocity for orthorhombic media. Geophysics 62 (4), 1292–1309.

Wang, N., Zhu, T., Zhou, H., et al., 2020. Fractional Laplacians viscoacoustic wavefield modeling with k-space-based time-stepping error compensating scheme. Geophysics 85 (1), T1–T13. https://doi.org/10.1190/geo2019-0151.1.

Wang, N., Xing, G., Zhu, T., et al., 2022a. Propagating seismic waves in VTI attenuating media using fractional viscoelastic wave equation. J. Geophys. Res. Solid Earth 127 (4). https://doi.org/10.1029/2021JB023280.

Wang, N., Shi, Y., Zhou, H., 2022b. Accurately stable Q-compensated reverse-time migration scheme for heterogeneous viscoelastic media. Rem. Sens. 14 (19), 4782. https://doi.org/10.3390/rs14194782.

Xu, S., Zhou, H., 2014. Accurate simulations of pure quasi-P-waves in complex anisotropic media. Geophysics 79 (6), T341–T348. https://doi.org/10.1190/geo2014-0242.1.

Xu, S., Stovas, A., Alkhalifah, T., Mikada, H., 2020. New acoustic approximation for transversely isotropic media with a vertical symmetry axis. Geophysics 85 (1), C1–C12. https://doi.org/10.1190/geo2019-0100.1.

Yoon, K., Suh, S., Ji, J., et al., 2010. Stability and speedup issues in TTI RTM implementation. In: 80th Annual International Meeting, SEG Expanded Abstracts, pp. 3221–3225.

Zhan, G., Pestana, R.C., Stoffa, P.L., 2012. Decoupled equations for reverse time migration in tilted transversely isotropic media. Geophysics 77 (2), T37–T45. https://doi.org/10.1190/geo2011-0175.1.

Zhang, H., Zhang, Y., 2008. Reverse time migration in 3D heterogeneous TTI media. In: 78th Annual International Meeting, SEG Expanded Abstracts, pp. 2196–2200. https://doi.org/10.1190/1.3059322.

Zhang, H., Zhang, G., Zhang, Y., 2009. Removing S-wave noise in TTI reverse time migration. In: 79th Annual International Meeting, SEG Expanded Abstracts, pp. 2849–2853. https://doi.org/10.1190/1.3255441.

Zhang, H., Zhang, Y., 2011. Reverse time migration in vertical and tilted orthorhombic media. In: 81th Annual International Meeting, SEG Expanded Abstracts, pp. 185–189. https://doi.org/10.1190/1.3627568.

Zhou, H., Zhang, G., Bloor, R., 2006a. An anisotropic acoustic wave equation for VTI media. In: 68th EAGE Conference and Exhibition Incorporating SPE EUROPEC, Expanded Abstracts. https://doi.org/10.3997/2214-4609.201402310 cp–2.

Zhou, H., Zhang, G., Bloor, R., 2006b. An anisotropic acoustic wave equation for modeling and migration in 2D TTI media. In: 76th Annual International Meeting, SEG Expanded Abstracts, pp. 194–198. https://doi.org/10.1190/1.2369913.